Open Ceramics 15 (2023) 100375

Contents lists available at ScienceDirect

Open Ceramics

journal homepage: www.sciencedirect.com/journal/open-ceramics

How is it possible to get optimal infiltration fronts during chemical vapor infiltration with thermal gradients ?

Gerard L. Vignoles [a,*], Cédric Descamps [a,b], Carole Charles [a,c], Christian Klein [a,d]

[a] U. Bordeaux, CNRS, CEA, Safran: Lab. for ThermoStructural Composites, LCTS, UMR 5801, 3, Allee La Boetie, Pessac, 33600, France
[b] Safran Ceramics, 105 Av. Marcel Dassault, Merignac, 33700, France
[c] ArianeGroup SAS, 3 rue de Touban, Le Haillan, 33185, France
[d] Safran Landing Systems, 7 Av. du Bel-Air, Villeurbanne, 69100, France

ARTICLE INFO

Handling Editor: Dr P Colombo

Keywords:
Chemical vapor infiltration
Process modeling
Ceramic-matrix composites

ABSTRACT

Introducing thermal gradients to improve the Chemical Vapor Infiltration (CVI) process is a key strategy to overcome its principal drawback, namely, the presence of residual porosity in the central part of ceramic composite material preforms.

The aim is to create an infiltration front starting from the least accessible part of the porous preform and progressing towards its surface. However, in practice, it may be quite difficult to evaluate the magnitude of the thermal gradient necessary for the achievement of this desired infiltration front. Modeling may bring solutions for the design of a successful processing situation. This paper reviews four distinct application examples, for which multi-physics numerical modeling studies have been developed and validated. These cases are also examined using analytical computations of a front infiltration criterion in order to discuss the influence of processing parameters on the quality of the process and of the resulting material.

1. Introduction

Ceramic-Matrix Composites (CMC) [1,2] and Carbon/Carbon (C/C) [3,4] Composites (also called Carbon-Fiber Reinforced Carbon - CF(R)C) are outstanding materials for highly demanding applications in which extreme mechanical, thermal and chemical loads are present. These materials consist in a reinforcement made of carbon or ceramic fibers [5] surrounded by a carbon or ceramic matrix, optionally in presence of an interphase located between the fibers and the matrix [6]. This composite structure confers them a non-brittle behavior with progressive damage during loading, therefore countering the largest weakness of ceramics as structural materials. Successful applications of C/C composites encompass aircraft braking discs [7], solid rocket motor throttles and divergents [8], thermal protection systems for atmospheric re-entry [9], ion thruster grids [10] and other applications in industry [11,12]. C/SiC composites [13] were designed to overcome the poor oxidation resistance of C/C composites, with successful applications as automotive braking discs [14], rocket nozzles [15], thermal protection systems, parts for industrial furnace management [16] and in aeronautic propulsion [17,18]. The development of SiC fibers has led to the emergence of SiC/SiC CMCs [19], with applications in aeronautic propulsion [20] and nuclear fission technology [21,22].

The development of non-oxide CMCs, featuring carbon or SiC matrices, is strongly linked to the Chemical Vapor Infiltration process [23–29]. Indeed, a better matrix quality is obtained through this process as compared to liquid-phase routes like Polymer Impregnation and Pyrolysis (PIP) [30] or Reactive Melt Infiltration (RMI)/Liquid Silicon Infiltration (LSI) processes [31,32], because matrix cracks are not generated and the fibers are not damaged by the intrusion of the potentially corrosive molten silicon [33]. On the other hand, CVI has the

Abbreviations: CMC, Ceramic-Matrix Composite; CVI, Chemical Vapor Infiltration; TG-CVI, Thermal-Gradient CVI; RF-CVI, CVI with Radio-Frequency heating; MW-CVI, CVI with Micro-Wave heating; PIP, Polymer Impregnation and Pyrolysis; MI, Melt Infiltration; RMI, Reactive Melt Infiltration; LSI, Liquid Silicon Infiltration; UHTCMC, Ultra-High Temperature CMC; FE, Finite Element (modeling method); E-CVI, Electrical heating CVI; H-CVI, Heaterless CVI; ODE, Ordinary DIfferential Equation; PDE, Partial Differential Equation; I-CVI, Isobaric, Isothermal CVI; F-CVI, Forced-flow CVI; C/C, Carbon/carbon composite; CFC, Carbon-Fiber reinforced Carbon; CFRC, Carbon-Fiber Reinforced Carbon; C/SiC, Carbon fiber/Silicon Carbide matrix composite; SiC/SiC, Silicon Carbide fiber/Silicon Carbide matrix composite.

* Corresponding author.
E-mail addresses: vinhola@lcts.u-bordeaux.fr (G.L. Vignoles), cedric.descamps@safrangroup.com (C. Descamps).

https://doi.org/10.1016/j.oceram.2023.100375
Received 26 December 2022; Received in revised form 22 April 2023; Accepted 17 May 2023
Available online 29 May 2023

important drawback, in addition to being an expensive and time-consuming process, of letting some residual porosity remain present in the as-processed composite, which can significantly lower its mechanical performance as compared to a fully dense composite [29]. So, one has to fight against the presence of residual porosity. One of the best ways to achieve this is to use thermal gradients in order to localize the deposition reaction precisely in the regions it does not have naturally a tendency to occur, *i.e.* in the center region of a composite part. This is the objective of Thermal-Gradient CVI (TG-CVI) which has been developed in several variations [26,34].

TG-CVI represents a significant time gain with respect to classical routes. It is already implemented in some industrial applications [35,36] and represents a promising future in the frame of aeronautic propulsion; moreover, its applications are now growing towards other domains.

It has been shown that, by using microwaves to enhance the CVI process [37,38], fabrication times can be reduced from several hundred hours to around 100 h [39,40] and down to only ≈ 25 h when RF-CVI is used to produce C_f-ultra high temperature ceramic matrix composites (UHTCMCs) [41]. Similar results were obtained with the MW-CVI pilot plant developed in the European project HELM for the production of SiC-based CMCs (HELM: High-frequency Electro-Magnetic technologies for advanced processing of ceramic matrix composites and graphite expansion) [42]. The Horizon 2020 project CEM-WAVE aims at developing with this technology both oxide and non-oxide CMC tube parts to replace metals in radiant combustion tubes used in secondary steelmaking. Indeed, the achievable processing cost reductions anticipated with the industrialization of MW-CVI (or any other TG-CVI variation) make these materials affordable in the cited application, because of their superior resistance to creep and corrosion, giving them larger lifetimes than their metallic competitors.

However, the overall cost of the process, its optimization, and sometimes even its control are important issues. This is why process modeling is of interest [43]. It can help in finding the best directions to improve the process efficiency while preserving or even improving the material quality, at a lower cost than carrying out systematic experimental explorations of the processing parameter space.

Many modeling works on variations of TG-CVI have been developed so far [44]. All of them are based on the solutions of balance equations for heat and species mass concentrations; some also incorporate electromagnetics in order to represent the heating system. These models span from simple 1D approximations [45–57] to complex, 2D or 3D Finite Element of Finite Volume analyzes [58–63]. Their raw results are temperature and mass deposition profiles or fields, for chosen processing conditions (reactor geometry, temperature, pressure, gas composition, porous preform characteristics). Comparative solutions for parameter variations help finding tendencies towards process optimization, *i.e.* lesser residual porosity at lowest energy and source gases expense. In addition to these classical approaches, a specific study on the existence and characteristics of a possible "infiltration front" has been made [56,64]. The front existence criterion is a good indication of the possibility of having an optimal inside-out infiltration in which the lowest possible residual porosity is obtained; moreover, its characteristics (thickness, velocity) are useful quantities for the actual implementation of the process. This front analysis has been compared to 1D FE simulations only in one case [56]. We propose further use in other situations, in order to grasp some more general understanding of the effects of process parameters on the infiltration quality.

This paper is structured as follows. First, we will recall some basic notions on the TG-CVI process, its modeling and the infiltration front analysis. Then, we will describe four practical application cases of TG-CVI involving C matrix infiltration; an analysis will be carried out for these cases using either FE simulation and/or front analysis. A final discussion will help drawing some conclusions and recommendations for future works.

2. TGCVI: principles and modeling

2.1. Process description

The general principle of CVI is the introduction of reactant gases inside a hot porous substrate, so that they deposit a solid by heterogeneous reaction [65]. Fig. 1 illustrates several variations of this concept. The basic implementation is the Isothermal-Isobaric CVI (or I-CVI), which does not involve temperature or pressure gradients; it has to be operated at low pressures in order to favor gas diffusion through the fibrous preform over the chemical reaction rate. As a consequence, processing times can be very long, which justifies the development of thermal-gradient variations. Bringing a thermal gradient can be achieved by using several distinct modes of injecting heat fluxes in the fibrous preform.

- Using the Joule effect brought by electrical currents circulating in a resistor [66,67].
- Using the preform itself to act as a heating resistor - this is E-CVI for Electrical-CVI or H-CVI for Heaterless-CVI [68,69].
- Creating the electrical current circulation inside the preform by induction, usually in the radio-frequency (kHz) range [61,70,71] - this is RF-CVI.
- Using microwave absorption [37,39,42,47,72,73] - this is MW-CVI.

Variations concerning the flow of gases are schematized in the lower right part of Fig. 1.

- The Forced CVI (F-CVI) in which the gases have to flow through the preform, generating a pressure gradient [74–76];
- The Film-Boiling CVI or "Kalamazoo" process in which the hot preform is immersed in the liquid precursor, ensuring a very large thermal gradient [24,77–80].
- The Supercritical CVI (or C–SCF–I) process in which the preform is heater electrically in a high-pressure reactor in order to increase the reaction kinetics [81].

2.2. Model bases: electromagnetism, heat and species mass balance equations

As it clearly appears in the description of these processes, there are four categories of phenomena that require modeling.

- Heating is provided by electrical power, either under the form of electrical conduction, RF induction or of microwave absorption. This involves the solution of electromagnetism equations which differ according to the main phenomenon: a simple Poisson equation may suffice for conduction, but for RF-CVI or MW-CVI, one needs to write down Maxwell's equations at least in partly simplified forms.
- Once the heat sources are known, the heat equation is used to describe heat transfer throughout the preform and with its surroundings.
- With knowledge of the temperature field, it becomes possible to describe the transport/reaction phenomena for the precursor gases and optionally for the by-product gases, inside the preform and optionally in the whole reactor cavity.
- Finally, the reaction rates being known, it is possible to describe the local solid deposition (or infiltration) rate; from this, updates to the porosity field can be made and a new step of the simulation can take place.

The couplings between the several segments of the model, which are linked to the main phenomena, are described in Fig. 2.

In principle, four types of equations have to be solved simultaneously; however, in practice, the evolution of the solid material is slow compared to all other transport phenomena, which allows decoupling

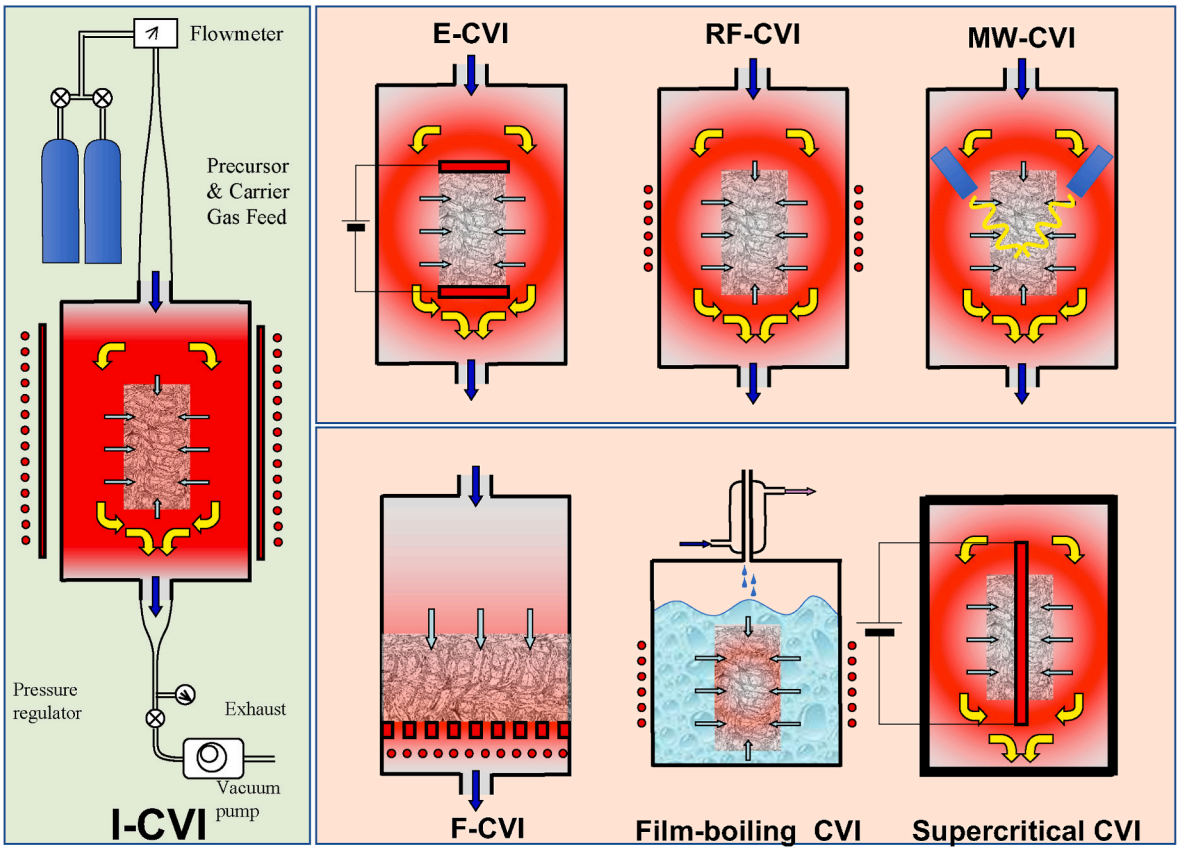

Fig. 1. Scheme of the basic I-CVI setup (left) and of TG-CVI variations (right). Top right: 3 variations differing by the heating mode; Bottom right: 3 variations differing by the gas circulation mode.

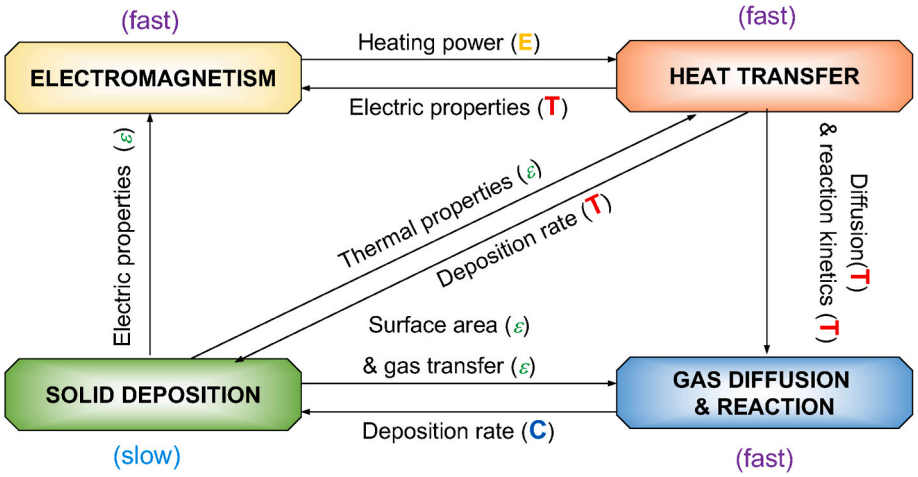

Fig. 2. Couplings between the main phenomena present in TG-CVI processes.

this last equation from the other ones, or at least to treat all equations but the solid mass balance as steady-state at a given infiltration stage. In 2D or 3D geometries, Finite Elements (FE) or Finite Volumes (FV) solvers may be conveniently used for the numerical solution of these coupled equations, which are essentially elliptic PDEs for the "pseudo-steady-state" equations for electromagnetic conduction or induction and for heat and mass balances and a simple ODE for solid mass balance. The details of these equations can be found *e.g.* in Ref. [44]; we will only recall here a basis set. The starting point, in any case, is the expression of the deposition rate:

$$R_{\mathrm{dep}} = \sigma_{\mathrm{v}}(\epsilon) k_{\mathrm{dep}}(T) C^{\alpha} \tag{1}$$

The internal surface depending on the porosity, the equation for the advancement of porosity is required:

$$-\frac{\partial \epsilon}{\partial t} = \frac{M_s}{\rho_s} R_{\mathrm{dep}} \tag{2}$$

The gas precursor concentration has to be determined everywhere, so this turns the species mass balance equation necessary for the model:

$$\nabla\cdot\left(\frac{P_i}{\mathscr{R}T}\mathbf{v}+\mathbf{J}_i^D\right)=R_{\text{dep}} \tag{3}$$

where the diffusive fluxes depend on the gas diffusivity, itself a function of porosity and, less importantly, of temperature. In TG-CVI, since the heterogeneous rate constant depends strongly on temperature, we see that the heat equation is necessary:

$$\rho c_p \mathbf{v}\cdot\nabla T+\nabla\cdot\mathbf{q_c}=S_h \tag{4}$$

where the heat capacity ρc_p and the conductive heat flux depend on the porosity and temperature. Here, we consider as negligible the effect of the heats of reaction, which has been verified for the deposition of C from C_xH_y-H_2 mixtures.

These three differential equations, in addition to eq. (1) and to the expressions of the heat and mass fluxes, constitute the minimal set for an investigation of infiltration in TG-CVI.

2.3. The "trilby hat effect"

All the above-mentioned CVI variants have the advantage of allowing to work with higher pressures, higher temperatures, and consequently higher rates and lower processing times. However, reports seem to indicate that such processes are somewhat difficult to control, and that undesired behavior may show up.

Indeed, reports on the "rapid process" [82] evidenced that, after a correct initial phase where densification would start from the hot side as expected, the density would eventually stop growing there, while keeping on increasing closer to the cold side. The resulting material has not an optimized density. Some runs of computed and measured infiltrations by the Georgia Tech team [52] also gave nonuniform density gradients, with a density maximum lying somewhere between the hot and the cold zone – if not sometimes at the cold side extremity. In the case of CVI with volume heating, a similar behavior occurred. Morell et al. [83] report a correct start of densification in the middle of the preform – as can be expected from the temperature field resulting from the balance between volume heating and surface radiative losses – followed by the break-up of a density maximum located in a circular region surrounding a less dense center, and finally by the propagation of a densification front towards the preform periphery. An MW-CVI model [45] and a more generic TG-CVI model [84] also showed the same feature. Fig. 3 schematizes this rather frequent scenario, that we can call "trilby-hat effect", due to the resulting shape of the density profile. We will see in the next sections that this effect can be understood as the unsuccessful construction of an infiltration front [64,84] at the beginning of the processing run.

2.4. Front analysis

The principle of the front analysis is in some way similar to the combustion front analyses of Zel'dovich and Frank-Kamenetskii [85] and of Novozhilov [86]. It is first assumed that a front exists and is moving at a (yet unknown) front velocity v_f. Then, a reference frame is chosen, focusing only the problem on the front zone. The set of three equations (2)–(4), of which 2 are PDEs, is transformed into a set of 3 ODEs if the only space coordinate along which the front progresses is retained. Suitable Cauchy conditions are specified on the left- and right-hand boundaries of the front zone, but they outnumber the number of ODEs to be solved. This is an over-determined problem, which becomes an eigenvalue problem, *i.e.*, a problem which only admits solutions for certain values of the parameters. This is also analogous to a "shooting problem". Here, the eigenvalues are the velocity and the front width. This problem has been solved by an iterative method based on dichotomy [56]. The front width and velocity can be approximated as:

$$\ell_f\approx\frac{\lambda_s T_h}{q}\frac{\mathscr{R}T_h}{E_a} \tag{5}$$

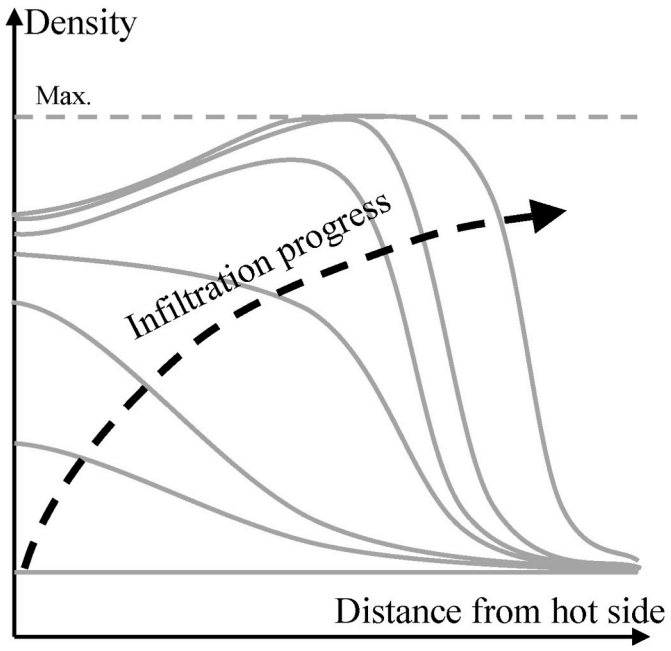

Fig. 3. Density evolution with time in many thermal-gradient CVI experiments: the "trilby-hat effect".

$$v_f\approx\ell_f A k_{dep}(T_h)\frac{M_s C_b}{\rho_s} \tag{6}$$

where T_h is the hot-side temperature of the front, λ_s, M_s and ρ_s the solid-phase conductivity, molar mass and density, C_b is the precursor concentration on the cold side, E_a is the deposition reaction activation energy and A an internal surface area scale parameter. More precisely, A is the slope of the $\sigma_v=f(\epsilon)$ (surface area *vs.* porosity) curve, evaluated at the end of infiltration (*i.e.* when $\sigma_v\to 0$); it is conveniently scaled by $\frac{1}{d_f}$, where d_f is a characteristic dimension of the fibers or of fiber bundles. In addition to these expressions of the front width and velocity, a front existence criterion has been derived. It may be expressed as the existence of a minimal heat flux:

$$q\geq\frac{\lambda_s\mathscr{R}T_h^2}{E_a}\sqrt{\frac{Ak_{dep}(T_h)}{D_g}}\cdot\frac{1}{\Phi_{\text{crit}}} \tag{7}$$

where D_g is a reference gas diffusion coefficient and Φ_{crit} is a critical Thiele modulus that can be computed from a local front simulation analysis. Another way of interpreting the criterion is the following:

$$\frac{v_f\ell_f}{D_g}\frac{\rho_s}{M_s C_b}\leq\Phi_{\text{crit}}^2 \tag{8}$$

Here, we recognize that the first fraction is a front-related reaction/diffusion ratio while the second one is a condensation ratio.

Combining eq. (7) and eqs. (5) and (6) yields the characteristic length and velocity of the critical front:

$$\ell_{f,\text{crit}}\approx\Phi_{\text{crit}}\sqrt{\frac{D_g}{Ak_{dep}(T_h)}} \tag{9}$$

$$v_{f,crit}\approx\Phi_{crit}\sqrt{D_g A k_{dep}(T_h)}\,\frac{M_s C_b}{\rho_s} \tag{10}$$

In practice, it may suffice to compute the critical heat flux at the initial condition, because the thermal gradient generally increases during process operation.

For a situation with a given preform width L_{pref}, hot-side temperature

T_h and cold-side temperature T_c, it can be assumed that the heat flux through the non-infiltrated ("dry") zone lying before the infiltration front can be written as:

$$q = \lambda_s(1-\epsilon_0)\frac{T_i - T_c}{L_{\text{dry}}} \tag{11}$$

where $L_{\text{dry}} = L_{\text{pref}} - \ell_{f,\text{crit}}$ and T_i is the deposition "ignition" temperature, *ie.* the minimal temperature above which the deposition rate is no more negligible. One can choose *eg.* an arbitrary criterion of $k_{\min} = 1.33 \cdot 10^{-8}$ m.s^{-1} for the rate constant, which gives a linear deposition rate of 0.1 μm in 24 h. For a simple Arrhenius law, one has:

$$T_i = \frac{E_a}{\mathscr{R}\ln\frac{k_0}{k_{min}}} \tag{12}$$

For an Arrhenius-Kooij law, all formulae can be retained, substituting E_a by $E_a^{'} = E_a + \beta\mathscr{R}T_h$. It is now possible to set a relationship between the largest preform dimension possible and the hot-side temperature, for a given cold-side temperature – which is the case in the Kalamazoo process. This dimension is:

$$L_{max} = \left(1 + (1-\epsilon_0)\frac{E_a^{'}\Phi_{\text{crit}}(T_i - T_c)}{\mathscr{R}T_h^2}\right)\sqrt{\frac{D_g}{Ak(T_h)}} \tag{13}$$

We will produce in the further sections some numerical estimates of these quantities.

3. Practical cases of TG-CVI

We will now discuss four different implementations of TG-CVI, all aimed at pyrolytic carbon matrix infiltration. They differ by the heating method, the reactor size and by the carbon precursor composition. Table 1 lists these cases. Fig. 4 provides sketches of the 4 experimental setups.

Case #1 has the largest dimensions of all cases; in it, the intention is to prepare C/C rocket nozzles. It involves plain CVI, using methane at low pressure (2.6 kPa) as a source gas. A multi-physics model of case #1 has been validated in Ref. [71].

In the next two cases, the film-boiling (or Kalamazoo) technique is employed, using liquid cyclohexane as a precursor. The contact of the preform with the boiling hydrocarbon helps maintaining a very strong thermal gradient. Case #2 has been extensively described in Ref. [79] and a multi-physics model has been proposed in Ref. [63].

Cases #1 and #3 are run in pilot-size reactors, in which the vessel dimensions are appreciably larger than the other two cases; for both, RF heating has been chosen as the most effective technique to achieve part heating. It is also attractive for being a contactless technique. Case #3 concerns a reactor capable of preparing a whole C/C brake disc; the preform thickness considered here is the half-width of the disc. The geometry of the inductive heating differs from case #3 to case #1, the latter case verifying a true axial cylindrical symmetry, whereas this is not achieved in case #3.

Case #4 has the particularity of using very high-pressure methane as precursor: the conditions can be called supercritical because indeed the critical pressure and temperature of methane are overtaken, but the process is operated in a parameter region where the perfect gas law holds [88]. It is otherwise quite similar to case #2: a vertical carbon resistor and a fibrous preform inserted around it in a cylindrical geometry.

All cases were run with preforms made of needled carbon fiber fabrics and/or non-woven plies. However, in case #2, two types of carbon preforms have been utilized: a very porous (> 90%) carbon fiber

Table 1
Description of the Thermal-Gradient CVI cases considered here.

Case	Reactor size	Preform thickness	Heating method	Carbon precursor	Refs.
#1	Pilot, Diam. 56 cm	135 mm	RF inductive heating	Methane (low pressure)	[71]
#2	Lab, Diam. 10 cm	15 mm	Contact with a hot resistor	Cyclohexane (liquid)	[79, 63]
#3	Pilot, Width 10 cm	35 mm	RF inductive heating	Cyclohexane (liquid)	[87]
#4	Lab, Diam. 7 cm	4.5 mm	Contact with a hot resistor	Methane (supercritical)	[81, 88]

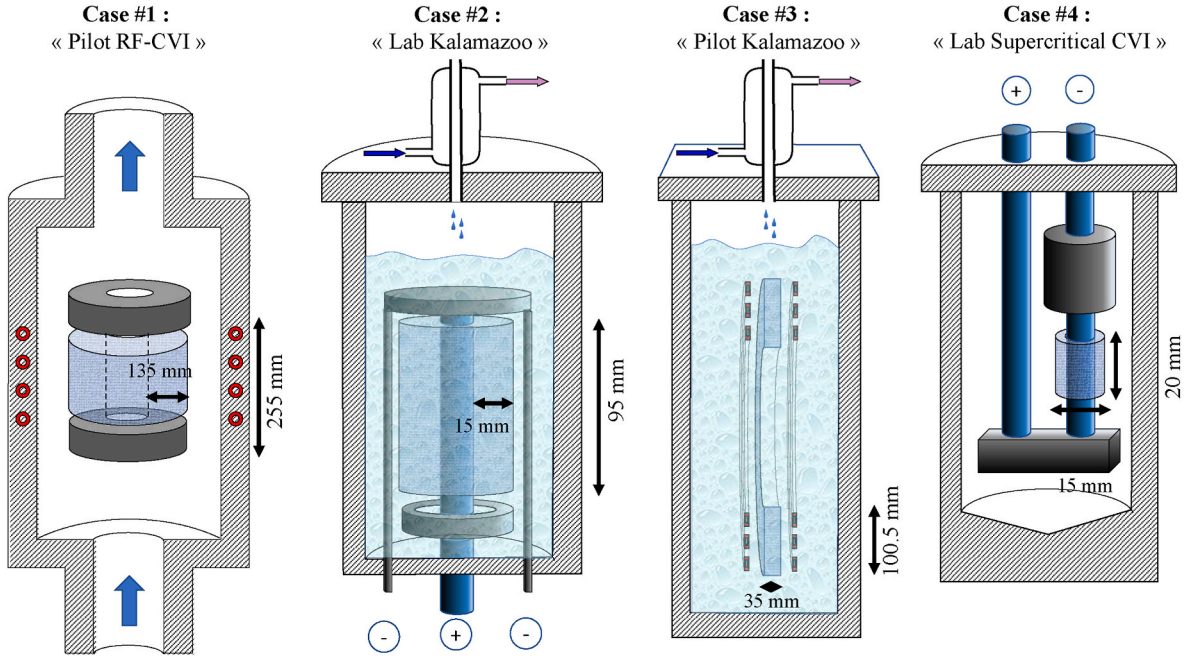

Fig. 4. Sketches of the 4 considered cases.

felt (RVC 2000 ® from (formerly) Carbone Lorraine), intended essentially to study the infiltration kinetics, and a less porous preform made of needled carbon fiber fabrics (Novoltex ® from (formerly) Snecma), in the aim of preparing useful carbon/carbon composites.

4. Analyses of the practical cases

4.1. The pilot-scale RF-CVI reactor: case #1

The multiphysics modeling of this reactor has been carried out using the following steps.

- First, the vector potential equation is solved in order to determine the power of the induced electric current present in the preform;
- Then, the energy equation is solved, in which the radiative heat losses are included as well as the input power.
- The Navier-Stokes equation is coupled to the heat equation for the gas outside the preform and both equations are solved again, using the previous results for initialization;
- Once the thermal landscape is set, the mass equations for gas precursor and solid deposit are solved, until the porosity has varied by a prescribed amount (*e.g.* 0.05)
- Go back to the first step and carry out the whole procedure again until final processing time.

Fig. 5 illustrates some steps of this procedure.

The computations confirmed the experimental observations of a "trilby-hat" effect, as illustrated in the right part of Fig. 5. This can be confirmed by comparing the actual heat flux and the critical flux given by the front existence criterion. Fig. 6 displays such a comparison, either with fixed hot-side (1325 K) and cold-side (873 K) temperatures, with varying preform half-width (Fig. 6 a)) or with fixed half-width and cold side temperature and varying hot-side temperature. It appears that the criterion is not initially satisfied (the critical flux is above the actual flux); however, if the half-width decreases, it is eventually met. This may explain the "trilby hat" effect. Fig. 6b) indicates that the criterion could also be initially met using a lower hot-side temperature; however, in these conditions, according to eq. (6), the front velocity would be more than 100 × slower.

4.2. The film-boiling (Kalamazoo) lab-scale reactor: case #2

The numerical model of this reactor could be restricted to a simultaneous solving of heat and gas species transfer equations, along with the solid deposit mass balance equation. Since there was a Joule heating of a central resistor, regulated thanks to a thermocouple, it has been sufficient to assign a fixed hot-side temperature on the inner diameter of the annular preform. Moreover, it has been found experimentally [79] that wrapping the preform with a thin Goretex® cloth had the effect of localizing the boiling zone at the preform boundary, or somewhere outside it (further computations have confirmed this fact [87]); as a consequence, modeling the phenomenon of precursor boiling inside the porous media was deemed unnecessary and replaced by a simple Fourier thermal boundary condition. Finally, because of the intense agitation of the fluid outside the preform, all boundary conditions for the gases could be treated as "fixed concentration" ones and the computational domain could be restricted to the preform only. The modeling approach has been successfully validated against experimental data in Refs. [63,89], using a very porous preform made of a carbon fiber felt. The results have shown a clear infiltration front, appearing immediately at the process start and migrating towards the cold side. However, when a needled fiber fabric stacking was used, the thermal gradient was much lower for the same heat flux and the infiltration front would not show up [79]. The reason was that the second type of porous medium is much less initially porous, therefore much more heat-conductive; moreover, its internal surface area is less important. Fig. 7 illustrates the comparison of the two structures, with a variation of the cold-side temperature while maintaining the hot side at 1373 K: clearly, using the first type of porous medium, the criterion is satisfied at the beginning of the process, whereas it is not the case with the other type of porous medium.

4.3. The film-boiling (Kalamazoo) pilot-scale reactor with induction heating: case #3

4.3.1. Direct numerical simulations

The difference between this case and the preceding one, apart from the geometry, comes from the heating method: here, direct RF induction is utilized (as in Case #1) instead of putting the preform in contact with a hot resistor. This has imposed to incorporate, as in Case #1, the solving of the EM equations. Moreover, the reactor was operated with resonance frequency tuning. The electrical circuit is schematized in Fig. 8; its main idea is as follows: (*i*) the induction coils and the preform are equivalent to an RL device. So, adding a condensator in parallel to it allows creating an oscillating subsystem. (*ii*) A transformer helps converting the frequency between the power grid input and the inductor system; it

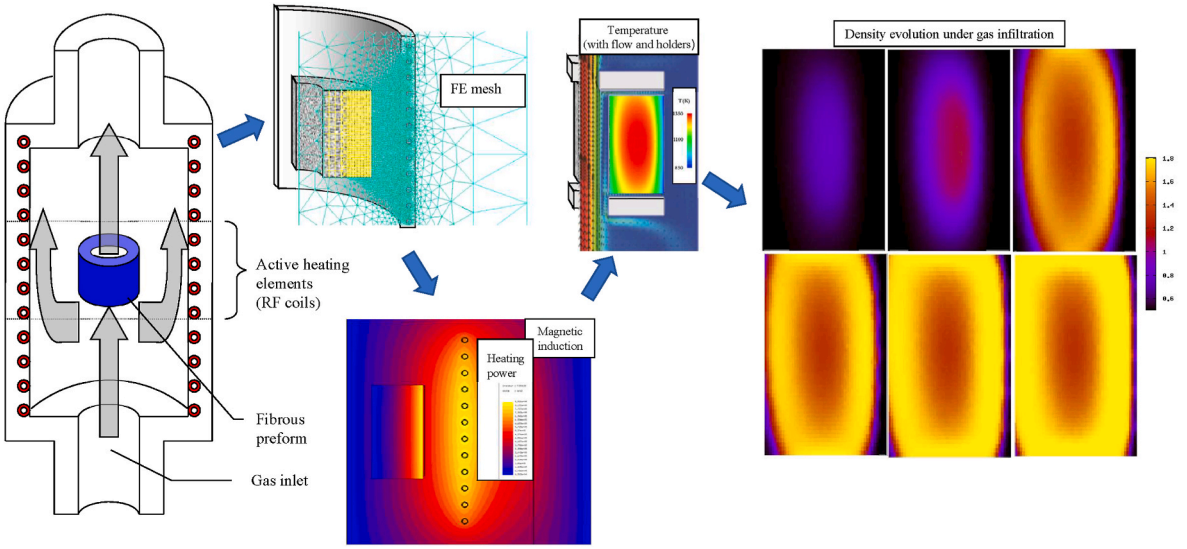

Fig. 5. Illustration of the multi-physics computational steps in Case #1.

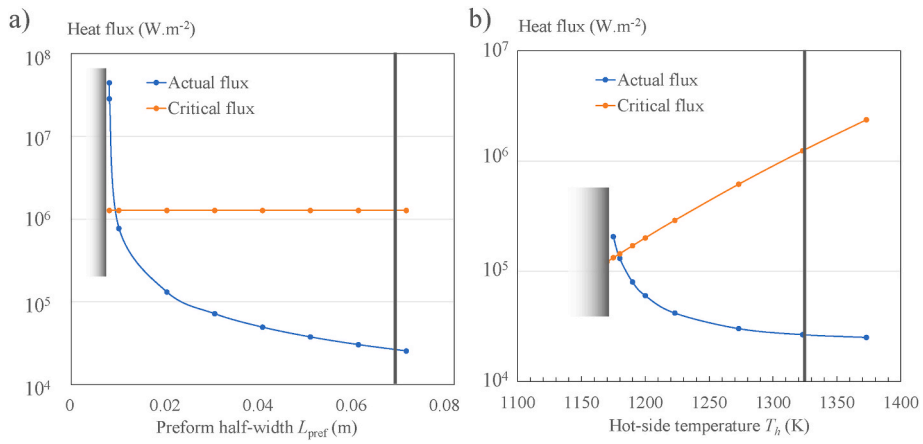

Fig. 6. Comparison of the actual heat flux and of the critical heat flux in Case #1. a) With variation of the preform half-width with fixed hot and cold temperature, b) with variable hot temperature and fixed cold temperature and half-width. Vertical dark lines refer to the reference case. On the left-hand side, the graphs are discontinued because the "actual flux" would diverge to infinity.

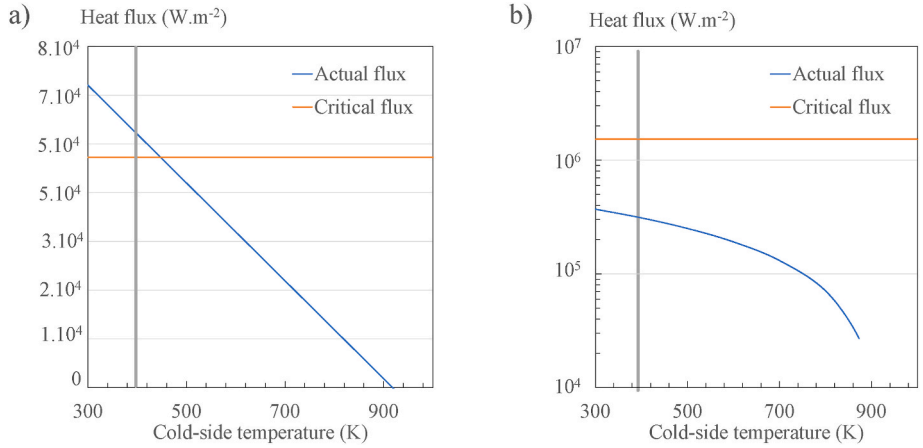

Fig. 7. Comparison of the actual heat flux and of the critical heat flux in Case #2, with variation of the cold temperature. a) with the RVC 2000 ® 94% porous felt of poorly conductive fibers, b) with the Novoltex ® needle-punched fabric stacking of more conductive fibers. Vertical grey lines refer to the reference case.

contains an undulator and an impedance adapter. The undulator frequency is tuned in order to obtain the resonance of the oscillating subsystem.

During simulation, a feedback loop has to be operated in order to determine at each infiltration step the value of the resonant frequency. To do so, two formulas will be used. First, the determination of the resonance frequency f_{res} as a function of the apparent electrokinetic properties R, L and C of the inductor-preform system:

$$f_{\text{res}} = \frac{\sqrt{1 - R^2 C/L}}{2\pi\sqrt{LC}} \tag{14}$$

While the capacity is a property of the exterior tuning system, the resistance R and inductance L of the inductor-preform system are obtained by post-processing the potential-vector field solved by FE on the computational domain. In cylindrical coordinates, one has:

$$R = \frac{Q_{rh}}{2\|I_{tot}\|^2} \tag{15}$$

$$Q_{rh} = 2\pi \iint_{\text{solids}} \sigma_e^{-1} \|j_\varphi\|^2 r dr dz \tag{16}$$

$$j_\varphi = -j\sigma_e \omega A_\varphi (1 - \varphi_{coil}) + \varphi_{coil} \frac{\sigma_{e,coil} U_{coil}}{2\pi r} \tag{17}$$

$$I_{tot} = \iint_{\text{solids}} j_\varphi dr dz \tag{18}$$

$$L = \frac{W_m}{2\|I_{tot}\|^2} \tag{19}$$

$$W_m = 2\pi \iint_{\text{domain}} \mu^{-1} \|\nabla \times \mathbf{A}\|^2 r dr dz \tag{20}$$

where Q_{rh} is the total Joule power loss, j_φ the local value of the electrical current density, φ_{coil} is a phase indicator of the coil (1 in coil, 0 outside), σ_e the electrical conductivity, U_{coil} the potential loss in the coil, I_{tot} the total circulating intensity, W_m is the magnetic field energy and μ the magnetic permeability.

The inductive heating efficiency may be computed as the ratio of the total energy produced by Joule effect in the preform divided by the total active power of the device (considered as an RL system):

$$\eta = \frac{Q_{rh}}{2\mathscr{R}\text{e}\left(\sum_{i=1}^{N_{coils}} U_{coil,i}\right) I} \tag{21}$$

The full simulation algorithm is sketched in Fig. 9.

Results of the simulation run are reported in Figs. (10) to (12). It is seen in Fig. (10) that the increase of the resonance frequency with time, almost linear, has been successfully reproduced, guaranteeing an almost

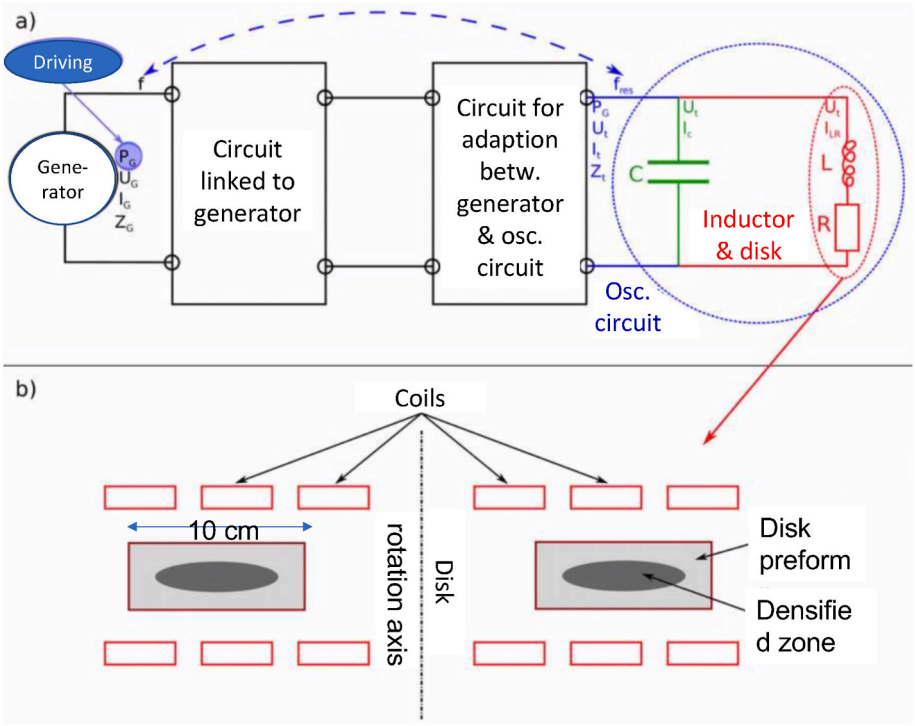

Fig. 8. Description of the RF heating system. a) Equivalent electrical circuit; b) the inductor-preform system, equivalent to an RL device.

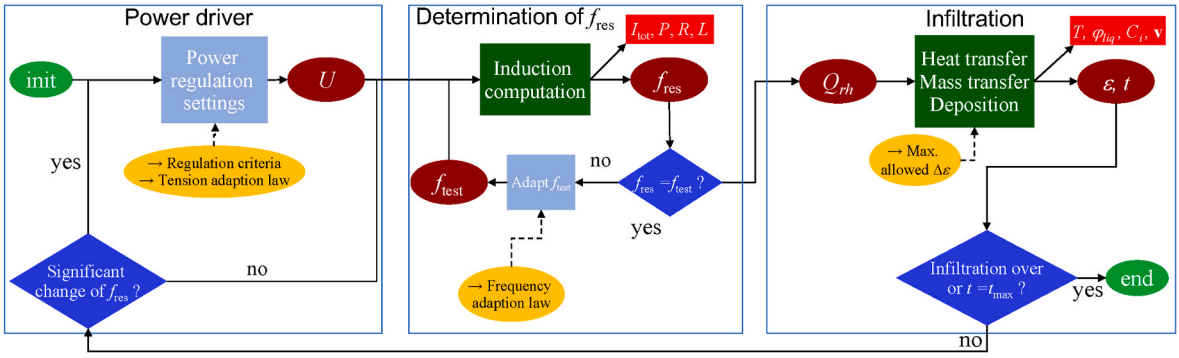

Fig. 9. Flowchart for a numerical simulation of the Kalamazoo process with RF heating, including a resonance frequency determination sub-loop.

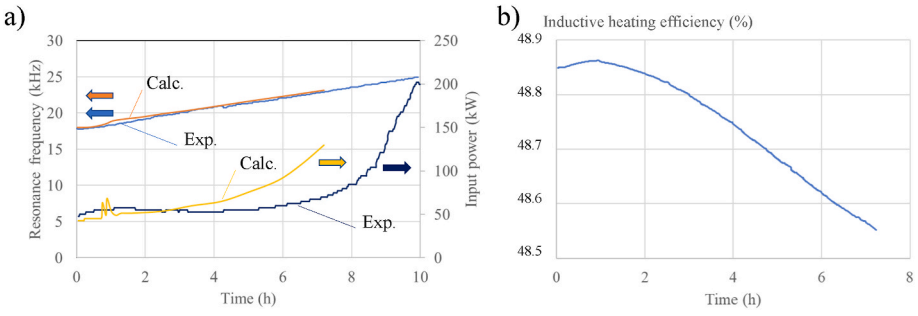

Fig. 10. Evolution with infiltration time of the RF inductive heating quantities. a) Left: experimental and computed resonance frequency and input power, b) Right: computed heating efficiency.

constant efficiency of the heating. On the other hand, the simulation tends to predict a too rapid increase of the input power, as compared to experiments. From a thermal viewpoint, it appears from Fig. (11) that the evolutions of the temperatures at selected locations have been quite well reproduced, with a notable exception at the top of the preform, a region where expulsion of the liquid from the preform has been predicted but not achieved experimentally, as opposed to the rest of the preform.

From the time evolutions of the temperature and porosity fields reported in Figure (12), it is seen that the infiltration reproduces again the

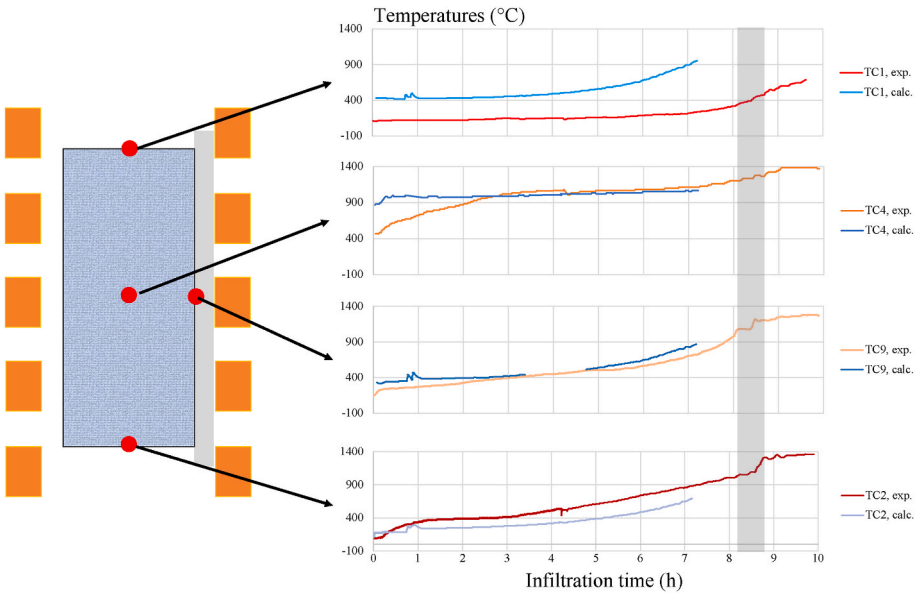

Fig. 11. Time evolution of the temperature recorded at several locations of the preform, marked by red circles. Experimental and computed thermograms are compared in the graphs. The shaded area in the time graphs corresponds to the moment where a film-boiling crisis is recorded in the region lying between the preform and the induction coils. (For interpretation of the references to color in this figure legend, the reader is referred to the Web version of this article.)

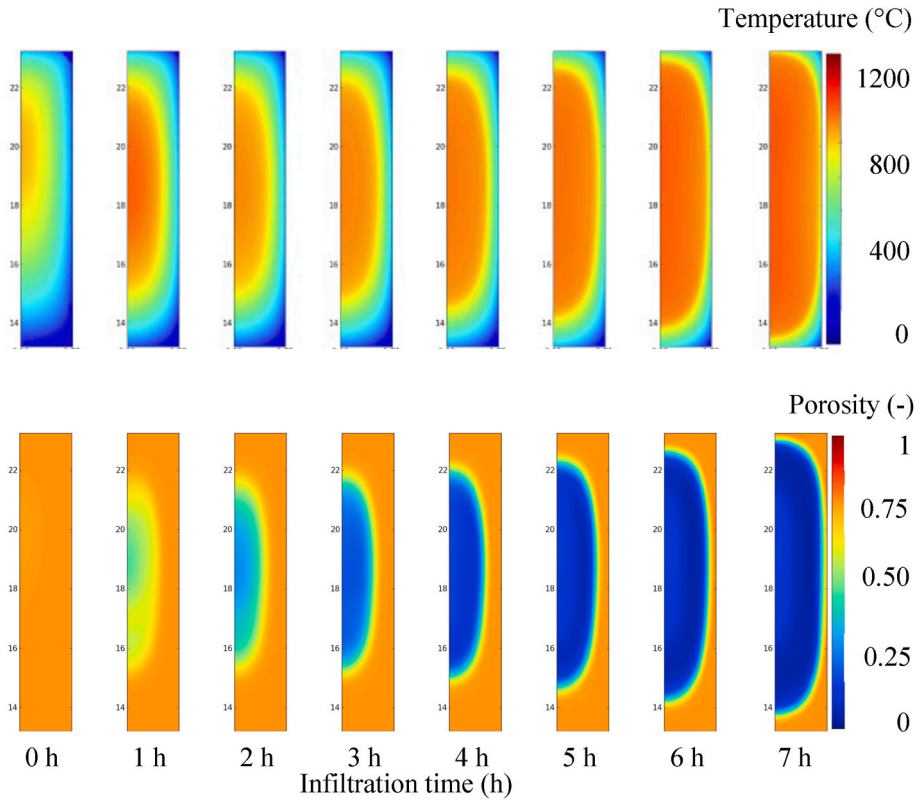

Fig. 12. Computed time evolutions of the temperature and the porosity.

"trilby hat" effect, though only with a slight depletion of the density in the middle of the preform section, accompanied by a strong decrease of the space gradient of temperature in the central region.

4.3.2. *Front existence analysis*

This simulation case, together with a preceding one, can be now re-examined using the analysis of the infiltration front existence and characteristics. In particular, relation (13) will be useful: for a given cold-side temperature, it provides an estimate of the maximum possible preform half-thickness for a front to exist. as a function of the hot-side temperature. Fig. 13 shows the curve associated to eq. (13) and the representative points of case #3 and of case #2b (*ie.* the Kalamazoo process with a Novoltex® preform, very similar to the one of case #3) have been inserted in the graph. Both representative points lie in the "no front" region, not very far away from the boundary of the front existence region. Case #3 lies closer to the boundary than case #2b, indicating

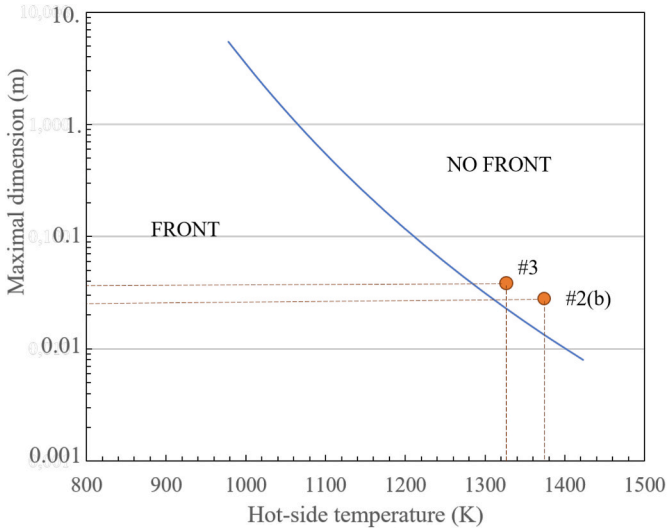

Fig. 13. Computation of the maximal possible half-width for front existence *vs.* hot-side temperature, for a cold-side temperature of 378 K, using eq. (13). The colored circles refer to the situations met in practice of cases #2 (with Novoltex ® preform) and #3.

that the criterion is only narrowly missed. – this is to relate to the fact that the non-optimal region (*ie.* the center part of the trilby hat) shows only a small depletion. Clearly, the graph of Fig. 13 indicates that for an optimized operation of the process, it would be necessary to lower the hot-side temperature while maintaining the same cold-side temperature. To do so, the heating power should be reduced but the total operation time would increase greatly, as suggested by eq. (10) in which the deposition constant has an Arrhenius-like temperature dependence: the critical front velocity also has an Arrhenius-like hot-side temperature dependence, though with half of the activation energy.

4.4. Case #4: the supercritical methane reactor

This process was first patented in 2006 [90] and described in a publication in 2014 [91]; a recent re-assessment of the process has been carried out [88], with a strong focus on thermal measurements. The detailed multi-physics model framework developed for the preceding cases has been adapted to the present one. The major modification was the chemical kinetic law, which has here to account for the reversibility of the deposition reaction. Indeed, very high pressures are bringing the system closer to thermochemical equilibrium between methane, hydrogen and carbon, so that the attack of carbon by hydrogen to give back hydrocarbons cannot be neglected any more. The proposed formalism is:

$$R = \sigma_v(\epsilon) k_{dep}(T) \left(\frac{P_m - P_{m,eq}}{\mathscr{R}T} \right) \tag{22}$$

where σ_v is the surface/volume ratio and $P_{m,eq}$ is the equilibrium partial pressure of methane, computed using a free enthalpy minimization program fed by a thermochemical database. The kinetic rate law constants A and E_a were determined from two sets of experiments: (*i*) CVD deposition experiments on a single filament, using directly eq. (22) for the interpretation and (*ii*) infiltration experiments, using the front formulas (5) and (6) (in which C_b has been replaced by $\frac{P_m - P_{m,eq}}{\mathscr{R}T}$) to retrieve $k_{dep}(T_h)$. Data obtained by these two methods were found giving results in coherence with each other and with past determinations obtained at ambient pressure. A remarkable result was the drop of the apparent activation energy from ≈ 280 kJ mol^{-1} at ambient pressure down to 70 kJ mol^{-1} at 50 bar, remaining then approximately constant for higher pressures.

Table 2
Actual and critical heat fluxes in supercritical CVI runs.

Run #	Hot-side temperature (K)	Heat flux (MW. m^{-2})	Critical heat flux (MW. m^{-2})
P3	1682	6.64	0.0648
P4	1698	7.97	0.0354
P6	1682	6.64	0.0848
P7	1698	7.97	0.0356
P8	1427	5.31	0.0444
P9	1682	6.64	0.0143
P10	1698	7.97	0.0526

Table 3
Summary of the results found on the 4 Thermal-Gradient CVI cases.

Case	Preform half-thickness (mm)	Front existence
#1	67.5	No
#2(a)	15	Yes (with felt)
#2(b)	15	No (with Novoltex ®)
#3	17.5	No
#4	4.5	Yes

The thermal study of the reactor evidenced a very steep thermal gradient, larger than could be initially expected from the readout of the temperature obtained from the thermocouple located in the center of the hollow heating tube. It was therefore no surprise that the infiltration occurred "inside-out" with a well-formed front. Indeed, even though the activation energy was rather low at high pressures, the criterion for front formation was met by 2 orders of magnitude, as shown in Table 2.

5. Summary and final discussion

We can now summarize in Table 3 the results of the experiments and simulations in the 4 practical cases described above.

Clearly, it can be seen from this synthesis that the existence of an infiltration front is achieved when the preform size is small enough; otherwise it becomes too difficult in practice to produce the necessary gradient. Another factor comes from the characteristics of the porous preform, as illustrated in case # 2: when it is not initially porous enough, the critical gradient is not reached.

We can go back to Eq. (13) which gives a maximal infiltrable thickness for given hot and cold-side temperatures, rewritten as:

$$L_{max} = \left(1 + (1 - \epsilon_0) \frac{E_a' \Phi_{\text{crit}} (T_i - T_c)}{\mathscr{R} T_h^2} \right) \sqrt{\frac{D_g}{A k_0}} \exp\left(\frac{E_a'}{2 \mathscr{R} T_h} \right) \tag{23}$$

In this equation, it is seen that the maximal infiltrable thickness, for a given chemical system and temperature gradient, relies on the initial porosity ϵ_0 and the surface area evolution factor A. We can also see that the activation energy has a negative influence on the maximal infiltrable thickness, whereas it has the beneficial effect of lowering the value of the critical gradient (see eq. (7)), as had been also found in the case of Temperature and Pressure pulsed CVI (TP-CVI) [92]. Lastly, it can be seen that increasing too much the hot-side temperature effect will affect negatively the efficiency of the process, because it will increase the critical flux and decrease the maximal infiltrable length. On the other hand, lowering the hot-side temperature has the detrimental effect of slowing down the process kinetics (see eqs. (6) and (10)).

6. Conclusion and perspectives

This document has focused on the comparison of 4 distinct practical cases of TG-CVI, featuring experimental data and modeling analysis through either detailed multiphysics FE simulations or estimates made by an analytical model of the infiltration front. The detailed numerical simulations have satisfactorily reproduced the experimental results and helped providing insights into the process as they are able to provide

access, in addition to verifiable data like thermograms or final density profiles, to inacessible data like the evolution of density during the whole process or the value of temperatures in inaccessible parts of the setup. A central point for the engineer is the capability of achieving inside-out infiltrations thanks to the existence of an infiltration front. It has been shown here that the criterion given by eq. (7) successfully predicts the front existence or, conversely, the existence of a "trilby-hat" effect. Such modeling tools are of importance for a proper up-scaling of the thermal-gradient CVI process. Unfortunately, they tend to show that increasing the thickness of the preform makes it harder to infitrate optimally. In principle, this can be overcome by lowering the hot-side temperature, at the expense of slowing down the whole infiltration process.

Future work on this topic includes the study of different setups, in particular with other chemical systems (*e.g.* SiC or Al_2O_3 deposition) and other heating modalities, such as micro-wave heating or localized laser heating in a "additive-manufacturing" fashion. These modeling tools could also renew the interest in temperature and/or pressure pulsing, by affording the capability of optimizing processing conditions.

Declaration of competing interest

The authors declare that they have no known competing financial interests or personal relationships that could have appeared to influence the work reported in this paper.

Acknowledgements

The authors are indebted to ArianeGroup SA for a PhD grant to C. C. and Safran Landing Systems for a PhD grant to C. K. G. L. V. acknowledges funding of parts of this work by the European Commission in the frame of the Horizon 2020 "CEM-WAVE" project (grant agreement no. 958170).

References

[1] W. Krenkel, Ceramic Matrix Composites: Fiber Reinforced Ceramics and Their Applications, John Wiley & Sons, Ltd, 2008, https://doi.org/10.1002/9783527622412.

[2] N.P. Bansal, J. Lamon (Eds.), Ceramic Matrix Composites: Materials, Modeling and Technology, John Wiley & Sons, Inc, 2014, https://doi.org/10.1002/9781118832998.

[3] G. Savage, Carbon/Carbon Composites, Chapman & Hall, London, 1993, https://doi.org/10.1007/978-94-011-1586-5.

[4] E. Fitzer, L.M. Manocha, Carbon Reinforcements and Carbon/Carbon Composites, Springer, 1998, https://doi.org/10.1007/978-3-642-58745-0.

[5] B. Clauß, Fibers for ceramic matrix composites, Chap. 1, in: W. Krenkel (Ed.), Ceramic Matrix Composites : Fiber Reinforced Ceramics and Their Applications, John Wiley & Sons, Ltd, 2008, pp. 1–20, https://doi.org/10.1002/9783527622412.ch1.

[6] J. Lamon, Interfaces and interphases, Chap. 3 in: W. Krenkel (Ed.), Ceramic Matrix Composites : Fiber Reinforced Ceramics and Their Applications, John Wiley & Sons, Ltd, 2008, pp. 49–68, doi:10.1002/9783527622412.ch3.

[7] W. Krenkel, J.G. Thébault, Ceramic matrix composites for friction applications, in: N.P. Bansal, J. Lamon (Eds.), Ceramic Matrix Composites 23, John Wiley & Sons, Ltd, 2014, pp. 647–671, https://doi.org/10.1002/9781118832998.ch23.

[8] M. Lacoste, A. Lacombe, P. Joyez, R.A. Ellis, J.C. Lee, F.M. Payne, Carbon/carbon extendible nozzles, Acta Astronaut. 50 (6) (2002) 357–367, https://doi.org/10.1016/S0094-5765(01)00178-3.

[9] G. Duffa, Ablative Thermal Protection Systems Modeling. AIAA Education Series, American Institute of Aeronautics and Astronautics, 2013, https://doi.org/10.2514/4.101717.

[10] I. Funaki, H. Kuninaka, K. Toki, Y. Shimizu, K. Nishiyama, Y. Horiuchi, Verification tests of carbon–carbon composite grids for microwave discharge ion thruster, J. Propul. Power 18 (1) (2002) 169–175, https://doi.org/10.2514/2.5913.

[11] H. Hatta, R. Weiß, P. David, Carbon/carbons and their industrial applications , Chap. 5 in: N.P. Bansal, J. Lamon (Eds.), Ceramic Matrix Composites : Materials, Modeling and Technology, John Wiley & Sons, Ltd., 2014, pp. 85–146, doi:10.1002/9781118832998.ch5.

[12] R. Weiß, Carbon/carbons and their industrial applications, Chap. 4, in: W. Krenkel (Ed.), Ceramic Matrix Composites : Fiber Reinforced Ceramics and Their Applications, John Wiley & Sons, Ltd., 2008, pp. 69–111, https://doi.org/10.1002/9783527622412.ch4.

[13] B. Heidenreich, Manufacture and applications of C/C-SiC and C/SiC composites, Ceram. Trans. 234 (2012) 183–198, https://doi.org/10.1002/9781118491867.ch20.

[14] W. Krenkel, R. Renz, CMCs for friction applications, chap. 16, in: W. Krenkel (Ed.), Ceramic Matrix Composites: Fiber Reinforced Ceramics and Their Applications, John Wiley & Sons, Ltd, 2008, pp. 385–407, https://doi.org/10.1002/9783527622412.ch16.

[15] F. Breede, R. Jemmali, H. Voggenreiter, D. Koch, Design and testing of a C/C-SiC nozzle extension manufactured via filament winding technique and liquid silicon infiltration, Ceram. Trans. 244 (2014) 3–14, https://doi.org/10.1002/9781118889770.ch1.

[16] B. Heidenreich, C/SiC and C/C-SiC composites, chap. 6, in: N.P. Bansal, J. Lamon (Eds.), Ceramic Matrix Composites: Materials, Modeling and Technology, John Wiley & Sons, Ltd, 2014, pp. 147–216, https://doi.org/10.1002/9781118832998.ch6.

[17] J.C. Cavalier, I. Berdoyes, E. Bouillon, Composites in aerospace industry, in: P. Vicenzini, M. Singh (Eds.), Advanced Inorganic Fibrous Composites V vol. 50 of Advances in Science and Technology, 2006, pp. 153–162. https://doi.org/10.4028/www.scientific.net/AST.50.153.

[18] F. Christin, CMC materials for space and aeronautical applications, chap. 14, in: W. Krenkel (Ed.), Ceramic Matrix Composites: Fiber Reinforced Ceramics and Their Applications, Wiley-VCH Verlag, 2008, pp. 327–352, https://doi.org/10.1002/9783527622412.ch14.

[19] R. Naslain, Design, preparation and properties of non-oxide CMCs for application in engines and nuclear reactors: an overview, Compos. Sci. Technol. 64 (2) (2004) 155–170, https://doi.org/10.1016/S0266-3538(03)00230-6.

[20] J.A. DiCarlo, Advances in SiC/SiC composites for aero-propulsion, chap. 18 in: N.P. Bansal, J. Lamon (Eds.), Ceramic Matrix Composites: Materials, Modeling and Technology, John Wiley & Sons, Inc., 2014, pp. 217–235, doi:10.1002/9781118832998.ch18.

[21] A. Kohyama, CMC for nuclear applications, chap. 15 in: W. Krenkel (Ed.), Ceramic Matrix Composites : Fiber Reinforced Ceramics and Their Applications, John Wiley & Sons, Ltd., 2008, pp. 353–384, doi:10.1002/9783527622412.ch15.

[22] C. Sauder, Ceramic matrix composites : nuclear applications, chap. 14, in: N. P. Bansal, J. Lamon (Eds.), Ceramic Matrix Composites: Materials, Modeling and Technology, John Wiley & Sons, Inc., 2014, pp. 609–646, https://doi.org/10.1002/9781118832998.ch14.

[23] T.M. Besmann, R.A. Lowden, D.P. Stinton, Overview of chemical vapor infiltration, in: R. Naslain, D. Doumeingts (Eds.), Proc. 1st Int. Conf. on High-Temperature Ceramic-Matrix Composites (HT-CMC). EACM, Woodhead, Cambridge, UK, 1993, pp. 215–229.

[24] P. Delhaès, Chemical vapor infiltration processes of carbon materials, chap. 5, in: P. Delhaès (Ed.), Fibers and Composites: vol. 2 of World of CarbonCRC Press/Taylor & Francis, London, 2003, pp. 87–111, https://doi.org/10.4324/9780203166789.

[25] A. Lazzeri, CVI processing of ceramic matrix composites, in: N.P. Bansal, A. R. Boccaccini (Eds.), Ceramics and Composites Processing Methods, John Wiley & Sons/The American Ceramic Society, New York, NY, USA, 2012, pp. 313–349, https://doi.org/10.1002/9781118176665.ch9.

[26] G.L. Vignoles, Chemical vapor deposition/infiltration processes for ceramic composites, chap. 8, in: P. Boisse (Ed.), Advances in Composites Manufacturing and Process Design, Elsevier Woodhead Scientific, 2016, pp. 147–176, https://doi.org/10.1016/B978-1-78242-307-2.00008-7.

[27] R. Naslain, R. Pailler, F. Langlais, A. Guette, S. Jacques, X-CVI (with X = I or P), a unique process for the engineering and infiltration of the interphase in *SiC*-matrix composites: an overview, of Ceramic Transactions. The American Ceramic Society 248 (2014) 391–401, https://doi.org/10.1002/9781118932995.ch42.

[28] F. Langlais, G.L. Vignoles, Chemical vapor infiltration processing of ceramic matrix composites, chap. 4, in: 2 nd ed, in: P.W.R. Beaumont, C.H. Zweben, M.B. Ruggles-Wrenn (Eds.), Comprehensive Composite Materials II, vol. 5, Elsevier, 2018, pp. 86–129, https://doi.org/10.1016/B978-0-12-803581-8.03912-6.

[29] D. Kopeliovich, Advances in manufacture of ceramic matrix composites by infiltration techniques, chap. 5, in: I.M. Low (Ed.), Advances in Ceramic Matrix Composites (Second Edition), second ed., Elsevier Inc, 2018, pp. 93–119, https://doi.org/10.1016/B978-0-08-102166-8.00005-0.

[30] R. Menendez, E. Casal, M. Granda, Liquid impregnation technique for carbon-carbon composites, chap. 7, in: P. Delhaès (Ed.), Fibers and Composites: vol. 2 of World of CarbonCRC Press/Taylor & Francis, London, 2003, pp. 139–156, https://doi.org/10.4324/9780203166789.

[31] G.S. Corman, K.L. Luthra, Silicon melt infiltrated ceramic composites (HiPerComp^{TM}), in: N.P. Bansal (Ed.), Handbook of Ceramic Composites, Springer US, Boston, MA, 2005, pp. 99–115, https://doi.org/10.1007/0-387-23986-3_5.

[32] F. Lenz, W. Krenkel, Carbon fiber reinforced ceramics based on reactive melt infiltration processes, J. Korean Ceram. Soc. 49 (4) (2012) 287–294, https://doi.org/10.4191/kcers.2012.49.4.287.

[33] M. Leuchs, Chemical vapour infiltration processes for ceramic matrix composites: manufacturing, properties, applications, chap. 6, in: W. Krenkel (Ed.), Ceramic Matrix Composites : Fiber Reinforced Ceramics and Their Applications, John Wiley & Sons, Ltd, 2008, pp. 141–164, https://doi.org/10.1002/9783527622412.ch6.

[34] Y.D. Xu, X.T. Yan, Chemical vapour infiltration, chap. 5, in: Chemical Vapour Deposition: an Integrated Engineering Design for Advanced Materials, Springer London, London, 2010, pp. 165–213, https://doi.org/10.1007/978-1-84882-894-0_5.

[35] F. Christin, Procédé d'infiltration chimique en phase vapeur d'un matériau au sein d'un substrat fibreux avec établissement d'un gradient de température dans celui-ci, 1995. French patent FR2711645(A1).

[36] I. Golecki, Rapid vapor-phase densification of refractory composites, Mater. Sci. Eng. Rep. R20 (2) (1997) 37–124, https://doi.org/10.1016/S0927-796X(97)00003-X.

[37] D.J. Devlin, R.P. Currier, R.S. Barbero, B.F. Espinoza, Chemical vapor infiltration with microwave heating, in: J.B. Wachtman J (Ed.), Proc. 17th Annual Conference on Composites and Advanced Ceramic Materials, vol. 14 of Ceram. Eng. Sci. Procs., The American Ceramic Society, Westerville, OH, 1993, pp. 761–767, https://doi.org/10.1002/9780470314234.ch9.

[38] D.J. Devlin, R.P. Currier, R.S. Barbero, B.F. Espinoza, Microwave assisted chemical vapor infiltration, in: T.M. Besmann, B.M. Gallois, J.W. Warren (Eds.), Chemical Vapor Deposition of Refractory Metals and Ceramics II; Vol. 250 of *Mater. Res. Soc. Online Proc. Lib*, Materials Research Society, Pittsburgh, Pennsylvania, 1991, pp. 245–250, https://doi.org/10.1557/PROC-250-245.

[39] D. Jaglin, J. Binner, B. Vaidhyanathan, C. Prentice, B. Shatwell, D. Grant, Microwave heated chemical vapor infiltration: densification mechanism of SiC_f/SiC composites, J. Am. Ceram. Soc. 89 (9) (2006) 2710–2717, https://doi.org/10.1111/j.1551-2916.2006.01127.x.

[40] J. Binner, B. Vaidhyanathan, D. Jaglin, Microwave heated chemical vapour infiltration of *SiC* powder impregnated *SiC* fibre preforms, Adv. Appl. Ceram. 112 (4) (2013) 235–241, https://doi.org/10.1179/1743676112Y.0000000071.

[41] V. Rubio, P. Ramanujam, D.K. Ramachandran, A. D'Angiò, J.G.P. Binner, Thermal ablation performance of C_f-HfB_2 composites with and without a C matrix deposited by CVI, in: M. Singh, T. Ohji, S. Dong, D. Koch, K. Shimamura, B. Clauß, B. Heidenreich, J. Akedo (Eds.), Advances in High Temperature Ceramic Matrix Composites and Materials for Sustainable Development, vol. 263 of Ceramic Transactions, John Wiley & Sons, Ltd., 2017, pp. 211–221, https://doi.org/10.1002/9781119407270.ch21.

[42] R. D'Ambrosio, L. Aliotta, V. Gigante, M. Coltelli, G. Annino, A. Lazzeri, Design of a pilot-scale microwave heated chemical vapor infiltration plant: an innovative approach, J. Eur. Ceram. Soc. 41 (5) (2021) 3019–3029, https://doi.org/10.1016/j.jeurceramsoc.2020.05.073.

[43] G.L. Vignoles, Modelling of the CVI processes, in: P. Vincenzini, M. Singh (Eds.), Advanced Inorganic Fibrous Composites V vol. 50 of Advances in Science and Technology, 2006, pp. 97–106. https://doi.org/10.4028/www.scientific.net/AST.50.97.

[44] G.L. Vignoles, Modeling of chemical vapor infiltration processes,, Chap. 17, in: P. Boisse (Ed.), Advances in Composites Manufacturing and Process Design, Elsevier Woodhead Scientific, 2016, pp. 415–458, https://doi.org/10.1016/B978-1-78242-307-2.00017-8.

[45] D. Gupta, J.W. Evans, A mathematical model for CVI with microwave heating and external cooling, J. Mater. Res. 6 (4) (1991) 810–818, https://doi.org/10.1557/JMR.1991.0810.

[46] J.I. Morell, D.J. Economou, N.R. Amundson, A mathematical model for chemical vapor infiltration with volume heating, J. Electrochem. Soc. 139 (1) (1992) 328–336, https://doi.org/10.1149/1.2069194.

[47] J.I. Morell, D.J. Economou, N.R. Amundson, Chemical vapor infiltration of *SiC* with microwave heating, J. Mater. Res. 8 (5) (1993) 1057–1067, https://doi.org/10.1557/JMR.1993.1057.

[48] M. Kawase, Y. Ikuta, T. Tago, T. Masuda, K. Hashimoto, Modeling of a thermal-gradient chemical vapor infiltration process for production of silicon carbide whisker/alumina composite, Chem. Eng. Sci. 49 (24A) (1994) 4861–4870, https://doi.org/10.1016/S0009-2509(05)80065-X.

[49] M.K. King, Modeling study of effects of temperature profiling on CVI processing of woven graphite preforms with dimethyldichlorosilane, J. Mater. Res. 9 (1994) 2174–2189, https://doi.org/10.1557/JMR.1994.2174.

[50] N. Tai, T. Chou, C. Ma, Effects of deposition mechanisms in the modeling of forced-flow/temperature-gradient chemical vapor infiltration, J. Am. Ceram. Soc. 77 (3) (1994) 849–851, https://doi.org/10.1111/j.1151-2916.1994.tb05378.x.

[51] J.Y. Ofori, S.V. Sotirchos, Dynamic convection-driven thermal gradient chemical vapor infiltration, J. Mater. Res. 11 (10) (1996) 2541–2555, https://doi.org/10.1557/JMR.1996.0320.

[52] S. Vaidyaraman, W. Lackey, P. Agrawal, T. Starr, 1-D model for forced flow-thermal gradient chemical vapor infiltration process for carbon/carbon composites, Carbon 34 (9) (1996) 1123–1133, https://doi.org/10.1016/0008-6223(96)00086-3.

[53] J.S. Lewis, W.J. Lackey, S. Vaidyaraman, Model for prediction of microstructure for carbon/carbon composites prepared by forced-flow -thermal gradient CVI, Carbon 35 (1) (1997) 103–112, https://doi.org/10.1016/S0008-6223(96)00121-2.

[54] D.J. Skamser, H.M. Jennings, D.L. Johnson, Model of chemical vapor infiltration using temperature gradients, J. Mater. Res. 12 (3) (1997) 724–737, https://doi.org/10.1557/JMR.1997.0107.

[55] B.S. Tilley, G.A. Kriegsmann, Microwave-enhanced chemical vapor infiltration: a sharp interface model, J. Eng. Mech. 41 (1) (2001) 33–54, https://doi.org/10.1023/A:1011816630517.

[56] N. Nadeau, G.L. Vignoles, C.M. Brauner, Analytical and numerical study of the densification of carbon/carbon composites by a film-boiling chemical vapor infiltration process, Chem. Eng. Sci. 61 (22) (2006) 7509–7527, https://doi.org/10.1016/j.ces.2006.08.027.

[57] D.K. Rollins, D.J. Rollins, A.D. Jones, Spatial-temporal semi-empirical dynamic modelling of thermal gradient CVI processes, Chem. Eng. Res. Des. 85 (10 A) (2007) 1390–1396, https://doi.org/10.1016/S0263-8762(07)73179-9.

[58] T.L. Starr, A.W. Smith, 3D modeling of forced flow thermal gradient CVI for ceramic composite fabrication, in: T.M. Besmann, B.M. Gallois (Eds.), Chemical Vapor Deposition of Refractory Metals and Ceramics: vol. 168 of Mat. Res. Soc. Symp. Proc., Materials Research Society, Pittsburgh, Pennsylvania, 1989, pp. 55–60, https://doi.org/10.1557/PROC-168-55.

[59] T. Tago, M. Kawase, Y. Ikuta, K. Hashimoto, Numerical simulation of the thermal-gradient chemical vapor infiltration process for production of fiber-reinforced ceramic composite, Chem. Eng. Sci. 56 (6) (2001) 2161–2170, https://doi.org/10.1016/S0009-2509(00)00492-9.

[60] D. Gupta, J.W. Evans, Mathematical model for chemical vapor infiltration in a microwave-heated preform, J. Am. Ceram. Soc. 76 (8) (1993) 1924–1932, https://doi.org/10.1111/j.1151-2916.1993.tb08313.x.

[61] V. Midha, D.J. Economou, A two-dimensional model of chemical vapor infiltration with radio frequency heating, J. Electrochem. Soc. 144 (11) (1997) 4062–4071, https://doi.org/10.1149/1.1838137.

[62] V. Midha, D.J. Economou, A two-dimensional model of chemical vapor infiltration with radio frequency heating. II. Strategies to achieve complete densification, J. Electrochem. Soc. 145 (10) (1998) 3569–3580, https://doi.org/10.1149/1.1838844.

[63] G.L. Vignoles, J.M. Goyhénèche, P. Sébastian, J.R. Puiggali, J.F. Lines, J. Lachaud, et al., The film-boiling densification process for *C/C* composite fabrication: from local scale to overall optimization, Chem. Eng. Sci. 61 (17) (2006) 5636–5653, https://doi.org/10.1016/j.ces.2006.04.025.

[64] G.L. Vignoles, N. Nadeau, C.M. Brauner, J.F. Lines, J.R. Puiggali, The notion of densification front in CVI processing with temperature gradients, in: E. Lara-Curzio, D. Zhu, W.M. Kriven (Eds.), Mechanical Properties and Performance of Engineering Ceramics and Composites, 26[2]of Ceramic Engineering and Science Proceedings, The American Ceramic Society, Westerville, OH, 2005, pp. 187–195, https://doi.org/10.1002/9780470291221.ch23.

[65] R. Bickerdike, A. Brown, G. Hughes, H. Ranson, The deposition of pyrolytic carbon in the pores of bonded and unbonded carbon powders, in: S. Mrozowski, M. L. Studebaker, P.L. Walker Jr. (Eds.), Procs. 5th Conf. on Carbon, vol. 1, Pergamon Press, New York, 1962, pp. 575–582. ISBN:9781483180533.

[66] J.G. Zhao, K.Z. Li, H.J. Li, C. Wang, The influence of thermal gradient on pyrocarbon deposition in carbon/carbon composites during the CVI process, Carbon 44 (4) (2006) 786–791, https://doi.org/10.1016/j.carbon.2005.08.030.

[67] Z. Ramadan, I.T. Im, Numerical study on heat transfer and densification for SiC composites during thermal gradient chemical vapour infiltration process, Carbon Letters 25 (1) (2018) 25–32, https://doi.org/10.5714/CL.2018.25.025.

[68] R.Y. Luo, Fabrication of carbon/carbon composites by an electrified preform heating CVI method, Carbon 40 (11) (2002) 1957–1963, https://doi.org/10.1016/S0008-6223(02)00027-1.

[69] S.F. Tang, J.Y. Deng, H.F. Du, W.C. Liu, K. Yang, Fabrication and microstructure of *C/SiC* composites using a novel heaterless chemical vapor infiltration technique, J. Am. Ceram. Soc. 88 (11) (2005) 3253–3255, https://doi.org/10.1111/j.1551-2916.2005.00571.x.

[70] D.J. Devlin, R.S. Barbero, K.N. Siebein, Radio frequency assisted chemical vapor infiltration, in: M.D. Allendorf, M. Robinson, R.K. Ulrich (Eds.), Chemical Vapor Deposition XIII; Vol. PV 96-5 of *the Electrochemical Society Proceedings Series*. The Electrochemical Society, 1996, pp. 571–577. Pennington, NJ.

[71] D. Leutard, G.L. Vignoles, F. Lamouroux, B. Bernard, Monitoring density and temperature in C/C composites elaborated by CVI with induction heating, J. Mater. Synth. Process. 9 (2001) 259–273, https://doi.org/10.1023/A:1015251518333. URL: https://hal.archives-ouvertes.fr/hal-00337419.

[72] D.J. Skamser, P.S. Day, H.M. Jennings, D.L. Johnson, Hybrid microwave-assisted chemical vapor infiltration of alumina fiber composites, in: J.B. Wachtman Jr. (Ed.), Proceedings of the 18th Annual Conference on Composites and Advanced Ceramic Materials—B: vol. 15[5] of Ceramic Engineering and Science Proceedings, John Wiley & Sons, Inc., 1994, pp. 916–923, https://doi.org/10.1002/9780470314555.ch38.

[73] M.S. Spotz, D.J. Skamser, P.S. Day, H.M. Jennings, D.L. Johnson, Microwave-assisted chemical vapor infiltration, in: J. B. Wachtman, Jr. (Ed.),Proceedings of the 17th Annual Conference on Composites and Advanced Ceramic Materials: vol. 14 of Ceramic Engineering and Science Proceedings, John Wiley & Sons, Inc., 2008, pp. 753–760, doi:10.1002/9780470314234.ch8.

[74] T. Gulden, J. Kaae, K. Norton, L. Thompson, Forced-flow thermal-gradient chemical vapor infiltration (CVI) of ceramic-matrix composites, in: K.E. Spear, G. W. Cullen (Eds.), Procs. 11th Intl. Conf. On CVD; Vol. 90-12 of *ECS Conf. Procs.* The Electrochem. Soc., The Electrochem. Soc., Pennington, NJ, USA, 1990, pp. 546–552.

[75] Y.G. Roman, C. Steijsiger, J. Gerretsen, R. Metselaar, The preparation of carbon reinforced silicon carbide composites using the isothermal forced flow chemical vapour infiltration technique, in: J.B. Wachtman Jr. (Ed.), Proceedings of the 17th Annual Conference on Composites and Advanced Ceramic Materials: vol. 14 of Ceramic Engineering and Science Proceedings, John Wiley & Sons, Inc., 2008, pp. 1190–1198, https://doi.org/10.1002/9780470314234.ch58.

[76] A. Pandey, P. Selvam, B. Dhindaw, S. Pati, Multiscale modeling of chemical vapor infiltration process for manufacturing of carbon-carbon composite, in: V. Srivastava, W. Krenkel, A. Pegoretti, C. Bowen (Eds.), Procs. Sixth International Conference on Recent Advances in Composite Materials, ICRACM-2019: vol. 21 of Materials Today: Proceedings, 2020, pp. 1059–1063, https://doi.org/10.1016/j.matpr.2020.01.005.

[77] M. Houdayer, J. Spitz, D. Tran Van, Process for the densification of a porous structure, US Patent no 4 (1984), 472 454.

[78] E. Bruneton, B. Narcy, A. Oberlin, Carbon-carbon composites prepared by a rapid densification process. I. Synthesis and physico-chemical data, Carbon 35 (10–11) (1997) 1593–1598, https://doi.org/10.1016/S0008-6223(97)00118-8.

[79] P. Delhaès, M. Trinquecoste, J.F. Lines, A. Cosculluela, J.M. Goyhénèche, M. Couzi, Chemical vapor infiltration of *C/C* composites : fast densification processes and matrix characterizations, Carbon 43 (2005) 681–691, https://doi.org/10.1016/j.carbon.2004.10.030.

[80] P. Delhaès, M. Trinquecoste, A. Derré, D. Rovillain, P. David, Film boiling chemical vapor infiltration of *C/C* composites : influence of mass and thermal transfers, Carbon Sci. 4 (4) (2003) 163–167. URL: https://koreascience.kr/article/JAKO200322463505368.pdf.

[81] L. Maillé, Y. Le Petitcorps, A. Guette, G. Vignoles, J. Roger, Synthesis of carbon coating and carbon matrix for c/c composites based on a hydrocarbon in its supercritical state, J. Supercrit. Fluids 127 (2017) 41–47, https://doi.org/10.1016/j.supflu.2017.03.015.

[82] I. Golecki, R.C. Morris, D. Narasimhan, N. Clements, Carbon-carbon composites inductively-heated and rapidly densified by thermal-gradient chemical vapor infiltration : density distributions and densification mechanism, in: K.V. Logan, Z. A. Munir, R.M. Spriggs (Eds.), Advanced Synthesis and Processing of Composites and Advanced Ceramics II; Vol. 79 of *Ceram. Trans.* The American Ceramic Society, The American Ceramic Society, Westerville, OH, 1996, pp. 135–142.

[83] J.I. Morell, D.J. Economou, N.R. Amundson, Pulsed-power volume-heating chemical vapor infiltration, J. Mater. Res. 7 (9) (1992) 2447–2457, https://doi.org/10.1557/JMR.1992.2447.

[84] R.R. Melkote, K.F. Jensen, A model for chemical vapor infiltration of fibrous substrates, in: T.M. Besmann, B.M. Gallois (Eds.), Chemical Vapor Deposition of Refractory Metals and Ceramics, vol. 168 of *Mater. Res. Soc. Symp. Proc.* Materials Research Society, Pittsburgh, PA, 1990, pp. 67–72. doi:10.1557/PROC-168-67.

[85] Y. Zel'dovich, D. Frank-Kamenetsky, Theory of flame propagation, Zh. Fiz. Khim. 12 (1938) 100–105.

[86] B.V. Novozhilov, Propagation rate of the front of an exothermic reaction in condensed phase, Dokl. Akad. Nauk SSSR 141 (1) (1961) 151–153. URL: http://mi.mathnet.ru/dan25737.

[87] C. Klein, Etude du procédé de densification par caléfaction de composites C/C, modélisation, optimisation du contrôle et du bilan énergétique [study of the film-boiling infiltration process of C/C composites; modelling, control and energy balance optimisations], thesis, University of Bordeaux, 2015. URL: http://www.theses.fr/2015BORD0231. URL:.

[88] G. Vignoles, L. Maillé, G. Talué, Q. Badey, A. Guette, R. Pailler, et al., Chemical supercritical fluid infiltration of pyrocarbon with thermal gradients: deposition kinetics and multiphysics modeling, J. Composit. Sci. 6 (1) (2022), https://doi.org/10.3390/jcs6010020, 22.

[89] J.F. Lines, G.L. Vignoles, J.M. Goyheneche, J.R. Puiggali, Thermal modelling of a carbon/carbon composite material fabrication process, J. Phys. IV 120 (2004) 291–297, https://doi.org/10.1051/jp4:2004120033.

[90] A. Guette, L. Maillé, N. Eberling-Fux, F. Christin, Procédé de formation d'un dépôt solide sur une surface d'un substrat ou au sein d'un substrat poreux, French patent FR2885542(B1), 2006.

[91] L. Maillé, A. Guette, R. Pailler, Y. Lepetitcorps, P. Weisbecker, Elaboration of C/C composites based on the infiltration of a hydrocarbon precursor in supercritical state into the preform, Powder Metall. Met Ceram. 52 (11–12) (2014) 669–673, https://doi.org/10.1007/s11106-014-9575-5.

[92] S. Bertrand, J.F. Lavaud, R. El-Hadi, G.L. Vignoles, R. Pailler, The thermal-gradient pulsed-power flow CVI process: a new chemical vapor infiltration technique for the densification of fibre preforms, J. Eur. Ceram. Soc. 18 (7) (1998) 857–870, https://doi.org/10.1016/S0955-2219(97)00210-0.